Observing Profiles of Derived Kinematic Field Quantities Using a Network of Profiling Sites

TIMOTHY J. WAGNER,[a] DAVID D. TURNER,[b] THIJS HEUS,[c] AND WILLIAM G. BLUMBERG[d]

[a] *Space Science and Engineering Center, University of Wisconsin–Madison, Madison, Wisconsin*
[b] *NOAA/Global Systems Laboratory, Boulder, Colorado*
[c] *Department of Physics, Cleveland State University, Cleveland, Ohio*
[d] *NASA Goddard Space Flight Center, Greenbelt, Maryland*

ABSTRACT: Observations of thermodynamic and kinematic parameters associated with derivatives of the thermodynamics and wind fields, namely, advection, vorticity, divergence, and deformation, can be obtained by applying Green's theorem to a network of observing sites. The five nodes that comprise the Atmospheric Radiation Measurement (ARM) Southern Great Plains (SGP) profiling network, spaced 50–80 km apart, are used to obtain measurements of these parameters over a finite region. To demonstrate the applicability of this technique at this location, it is first applied to gridded model output from the High-Resolution Rapid Refresh (HRRR) numerical weather prediction model, using profiles from the locations of ARM network sites, so that values calculated from this method can be directly compared to finite difference calculations. Good agreement is found between both approaches as well as between the model and values calculated from the observations. Uncertainties for the observations are obtained via a Monte Carlo process in which the profiles are randomly perturbed in accordance with their known error characteristics. The existing size of the ARM network is well suited to capturing these parameters, with strong correlations to model values and smaller uncertainties than a more closely spaced network, yet it is small enough that it avoids the tendency for advection to go to zero over a large area.

KEYWORDS: Advection; Convergence/divergence; Vorticity; Kinematics; Lidars/Lidar observations; Profilers, atmospheric; Sampling

1. Introduction

The application of concepts from fluid mechanics and dynamics has been an important part of the atmospheric sciences for generations. It is well known that the atmosphere behaves as a fluid, and so fundamental tools like the material (or Lagrangian) derivative and the Laplacian operator have found important roles to play in our conceptualization of the atmosphere and its behavior across length and time scales. Applying these tools to wind and scalar fields to produce familiar concepts like vorticity, divergence, deformation, and advection has enabled a greater understanding of the fundamentals of a wide panoply of atmospheric phenomena at the most foundational level, from cyclones (e.g., Sutcliffe 1939) to frontogenesis (e.g., Petterssen 1936) to severe convection (e.g., Rotunno and Klemp 1985). Advection is of particular interest, as it is an important part of closing the energy and moisture budgets of a given environment (Santanello et al. 2009). Observations of the rate of change of scalar quantities like temperature or water vapor include both the change due to advection as well as the local change caused by land surface–atmosphere interactions and other effects, and it can be difficult to disentangle contributions of the latter without knowledge of the former.

Direct observations of these field quantities can often be challenging, however, which can limit their use by both operational forecasters and researchers. Quantifications of these derived quantities are often accomplished using numerical weather prediction (NWP) output. Since NWP analyses and forecasts produce spatial fields that vary smoothly over a regular grid, it is not difficult to use finite differences or other methods to calculate the gradients and higher-order derivatives required to obtain the magnitudes of these parameters. Of course, models have limited temporal resolution and do not perfectly represent the atmosphere, which means that real-world observations of these parameters can capture processes and phenomena that models cannot. Unfortunately, real-world observations are rarely distributed on a grid, and thus, methods more sophisticated than finite differencing are required to determine these derived quantities. While it may be tempting to project the observations onto a Cartesian grid to facilitate these calculations, it has been shown that doing so introduces discontinuities that can force substantial errors when calculating gradients (Spencer and Doswell 2001).

Instead, scientists have applied vector calculus methods to perform these calculations. Green's theorem, a method of relating line integrals to spatial derivatives, has been shown via simulated observations to be capable of producing accurate calculations of wind field kinematics (Zamora et al. 1987; Davies-Jones 1993) as well as advection (Michael 1994). Real-world applications of this method include calculating vorticity from Quick Scatterometer wind data (Bourassa and Ford 2010) and from dropsondes (Helms and Hart 2012, 2013; Bony and Stevens 2019).

The application of these or functionally identical techniques (such as the linear vector point function) for the calculation of wind field kinematics has previously been demonstrated on

Corresponding author: Timothy J. Wagner, tim.wagner@ssec.wisc.edu

the formerly operational NOAA Profiler Network, a system of radar wind profilers that operated at 404 MHz and deployed at approximately 30 sites in the central United States prior to its decommissioning in the early 2000s. While it was shown that this network could be used for vorticity, divergence, and deformation (e.g., Zamora et al. 1987; Carlson and Forbes 1989; Spencer et al. 1999), most of the sites had no thermodynamic profiling capabilities, and thus, the ability to continuously measure profiles of temperature or moisture advection remained underexplored.

In the present work, these prior approaches are applied to the profiles of lower tropospheric temperature, water vapor, and horizontal wind vectors that are observed nearly continuously at the Southern Great Plains (SGP; Sisterson et al. 2016) site of the Atmospheric Radiation Measurement (ARM) climate research facility so that temporally continuous profiles of advection and other field quantities can be observed. With Doppler lidar wind profilers and infrared thermodynamic profilers collocated at five separate sites, this network is well suited toward monitoring the evolution of the vertical state of advection and wind field kinematics of the PBL in unprecedented detail. To assess the utility of a line-integral-based approach at the SGP site, this paper first uses model analysis data as a proxy for real-world conditions to compare these calculations with more traditional methods and then explores the impact that the number of instruments, their locations, and their uncertainty can have on the results. The approach is then expanded to include the real-world data from the ARM SGP network, and the impact that the uncertainties of those instruments have on the calculations is quantified.

2. Methodology

This method of calculating the wind field properties draws upon concepts from vector calculus, especially Green's theorem, which can be depicted as

$$\oint_C P\,dx + Q\,dy = \iint \left(\frac{\partial Q}{\partial x} - \frac{\partial P}{\partial y}\right) dA, \qquad (1)$$

where P and Q are arbitrary smoothly varying variables lying in a region bounded by the circuit C and having area A. By approximating the line integral as a sum of finite line segments with mean values obtained using the endpoints of each segment it is possible to restate this as

$$\frac{\partial Q}{\partial x} - \frac{\partial P}{\partial y} \approx \frac{\sum \left(\overline{P}\Delta x + \overline{Q}\Delta y\right)}{A}, \qquad (2)$$

where Δx and Δy are the zonal and meridional components of the line segments comprising the edge of the region. Since exact definitions of vorticity, divergence, and deformation can all be obtained from the left-hand side of (2) when the proper arrangement of $\pm u$ and $\pm v$ (the zonal and meridional components of wind, respectively) is substituted for P or Q, measures of these quantities can be obtained from irregularly spaced observations so long as a polygon with finite sides can

be drawn using the locations of the observations at its vertices (thus requiring at least three noncollinear observation sites) and the mean values along those sides can be determined (Helms and Hart 2013). One merely needs to determine the value of the parenthetical term for each side of the polygon, sum over all sides of the polygon, and divide by its area.

A similar approach can be taken for advection of a scalar quantity. It is well known that the observed change in a scalar quantity at a fixed location is due to two causes: first, the change in the quantity following the air parcel; and second, the change due to advection of parcels with different values from other locations to the current one. This is expressed in the familiar expression for the material derivative

$$\frac{\partial \alpha}{\partial t} = \frac{D\alpha}{Dt} - \mathbf{V} \cdot \nabla \alpha, \qquad (3)$$

where α is an arbitrary scalar and $\mathbf{V}$ is the horizontal velocity vector. The $-\mathbf{V} \cdot \nabla \alpha$ term in (3) represents the advective portion of the change, and through basic vector arithmetic can be expanded to

$$-\mathbf{V} \cdot \nabla \alpha = -\left(u\,\frac{\partial \alpha}{\partial x} + v\,\frac{\partial \alpha}{\partial y}\right). \qquad (4)$$

The parallels between the right-hand side of (4) and the left-hand side of (2) are obvious, and so a Green's theorem–based approach can also be developed to calculate advection from a network of observing sites (Michael 1994). Critically, it was determined through testing that the mean scalar value of the polygon vertices needed to be removed from each scalar observation prior to calculating the advection in order to produce a properly scaled result. For example, an advective tendency of 1.0 K h^{-1} is identical to 1.0°C h^{-1}. However, due to the dependence of the calculation on the magnitude of the scalar, calculations performed on observations in kelvin will produce more extreme advection values than those performed on the same observations after conversion to Celsius. Subtracting out the mean value of the polygon vertices results in equivalent values for both scales that also align with model output. Table 1 summarizes the proper substitutions necessary in (2) to produce desired spatially derived kinematic and advective quantities.

3. Experiment domain and instrumentation

The Department of Energy's ARM SGP site is one of the most comprehensive atmospheric observatories in the world, hosting continuous observations of atmospheric, cloud, aerosol, and radiative properties for over 25 years (Turner and Ellingson 2016). The domain of the site extends beyond the borders of the well-known central facility in north central Oklahoma to include numerous observation sites throughout northern Oklahoma and southern Kansas. Four extended facilities (EFs) are a key part of this arrangement. Each of these four EF sites is approximately 40–50 km from the central facility and together they form a rough rectangle approximately 70 km in the east–west direction and 60 km in the north–south direction with the central facility at its center

TABLE 1. Equations of approximations for spatially derived kinematic and advective quantities. Overbars represent the mean values along a given segment of the polygon using the observed values at the end of that line segment (the vertices of the polygon). The primes for the scalar quantities in the advection calculations represent the residual scalar values after the mean value at all vertices has been removed. While the right-hand side of the advection equations includes a term that calculates the mean of the residuals along one side, each side includes only two points. The residuals were calculated relative to three or more points, and so this term typically does not resolve to zero. After Helms and Hart (2013).

Parameter	P	Q	Equation
Vertical vorticity	u	v	$\zeta = \dfrac{\partial v}{\partial x} - \dfrac{\partial u}{\partial y} \approx \dfrac{\sum(\bar{u}\Delta x + \bar{v}\Delta y)}{A}$
Divergence	$-v$	u	$D = \dfrac{\partial u}{\partial x} + \dfrac{\partial v}{\partial y} \approx \dfrac{\sum(\bar{u}\Delta y - \bar{v}\Delta x)}{A}$
Stretching deformation	v	u	$F_1 = \dfrac{\partial u}{\partial x} - \dfrac{\partial v}{\partial y} \approx \dfrac{\sum(\bar{v}\Delta x + \bar{u}\Delta y)}{A}$
Shearing deformation	$-u$	v	$F_2 = \dfrac{\partial v}{\partial x} + \dfrac{\partial u}{\partial y} \approx \dfrac{\sum(\bar{v}\Delta y - \bar{u}\Delta x)}{A}$
Temperature advection	$-T'v$	$T'u$	$-\mathbf{V} \cdot \nabla T = -\left(u\dfrac{\partial T'}{\partial x} + v\dfrac{\partial T'}{\partial y}\right) \approx \dfrac{-\sum \overline{T'}(\bar{u}\Delta y - \bar{v}\Delta x)}{A}$
Moisture advection	$-q'v$	$q'u$	$-\mathbf{V} \cdot \nabla q = -\left(u\dfrac{\partial q'}{\partial x} + v\dfrac{\partial q'}{\partial y}\right) \approx \dfrac{-\sum \overline{q'}(\bar{u}\Delta y - \bar{v}\Delta x)}{A}$

(Fig. 1). Along with the central facility, these sites host ground-based high-temporal-resolution thermodynamic and kinematic profilers in support of large-eddy simulation (LES) model initialization and evaluation, cloud and radiative process studies, and other scientific purposes. The surface cover throughout this domain is far from homogeneous. The northeastern section is characterized by deciduous forest, the southeastern by pasture, and the remainder of the domain is dominated by winter wheat, with peak greenness in midspring (Blumberg et al. 2019).

All five nodes of this profiling network contain a Halo Photonics Streamline Doppler lidar (DLID; Pearson et al. 2009), a 1.5-μm pulsed lidar from which profiles of the three-

FIG. 1. Map of the ARM SGP domain, including the location of the Central Facility (C1) and the four extended facilities (locations starting with "E"), along with elevations (in m). The inset map shows the location of the domain within the state of Oklahoma.

dimensional wind vector can be obtained using the velocity–azimuth display (VAD) technique. While the DLIDs have a maximum unambiguous range of several kilometers, the lidars require scatterers to return the signal to the instrument and facilitate an observation. This practically limits the observations to roughly the lowest 1.5 km of the troposphere, depending on the depth of the planetary boundary layer and the number of scatterers present, and the height of the maximum extent of the profile can vary from one observation time to the next. Four of the five sites also contain an Atmospheric Emitted Radiance Interferometer (AERI; Knuteson et al. 2004a,b), a high-spectral-resolution (better than 1 cm^{-1}) infrared radiometer that passively observes downwelling spectra in the thermal infrared. The fifth site (E41; Fig. 1) was instead until recently home to an Atmospheric Sounder Spectrometer for Infrared Spectral Technology (ASSIST; Rochette et al. 2009), an AERI-like instrument that produces similar high-spectral-resolution radiance observations.

Retrievals of the temperature and water vapor profiles from the AERI and ASSIST were obtained from the Tropospheric Remotely Observed Profiling via Optimal Estimation retrieval (TROPoe; formerly known as AERIoe; Turner and Löhnert 2014; Turner and Blumberg 2019) algorithm. TROPoe uses the Line-by-Line Radiative Transfer Model (LBLRTM) (Clough et al. 2005) as the forward model in a Gauss–Newton optimal estimation scheme (Rodgers 2000). The a priori for the retrieval was derived from a decade-long dataset of radiosondes launched four times daily from the SGP Central Facility; only sondes from the calendar month of the retrieval as well as one calendar month before and after are used when generating the a priori to insure its representativeness of the present environment. While TROPoe was designed for use on AERI radiances, its open design and radiative transfer model–agnostic architecture enable it to be used for retrievals on a variety of different infrared and microwave instruments, including ASSIST as was done in the
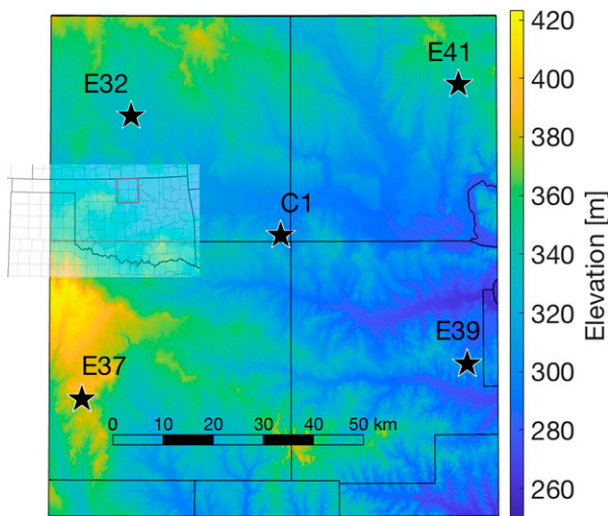
present work. (Hereafter, when this paper refers to the AERI profiles, that also includes the profiles retrieved with the TROPoe algorithm from the ASSIST spectra.) The information content present in the infrared spectrum decreases exponentially with height, with effectively no additional information added at heights more than 3 km above ground level; this is well beyond the effective maximum range of the DLID. Since clouds are optically thick at infrared wavelengths, no new information can come from within or above the cloud and so TROPoe effectively only retrieves up to cloud base when clouds are present. No retrievals are possible during precipitating conditions due to the strong infrared emittance of raindrops; at these times an automated hatch covers the instrument foreoptics to protect them.

It is imperative for observations of the atmosphere to include some measure of uncertainty. Since the advection algorithm requires the use of two different types of instruments (AERI and DLID) each with their own error characteristics, a method of integrating these individual uncertainties into a total instrument uncertainty for the retrieved product needed to be developed. A TROPoe retrieval includes a full posterior error covariance matrix, which includes the contributions from both the uncertainty in the radiance observations, the uncertainty in the a priori, and the sensitivity of the forward model used in the retrieval. Since thermodynamic retrievals are an ill-posed problem, the solution state is an attempt to find the statistically most likely solution for a given spectral observation. However, within the limits of the uncertainty of the observed spectra, an infinite number of solutions are mathematically valid. The derived uncertainty can be used to reconstruct additional valid profiles from the solution state using the following equation (Rodgers 2000):

$$\hat{\mathbf{X}} = \mathbf{S}^{1/2}\mathbf{Z} + \mathbf{X}, \qquad (5)$$

where $\hat{\mathbf{X}}$ is the perturbed profile, $\mathbf{X}$ is the retrieved profile, $\mathbf{S}$ is the posterior covariance matrix, and $\mathbf{Z}$ is a vector of normally distributed random numbers (one for each level of the profile) drawn from a distribution with a mean of zero and a standard deviation of 1. Through repeated Monte Carlo sampling, additional valid solutions can be generated with each solution lying within the envelope of uncertainty and the vertical correlations between the various levels remaining intact.

Since the wind observations lack posterior covariance matrices, the approach for handing instrument uncertainty was more straightforward. The DLID wind profiler data product generated by the ARM program contains one-sigma uncertainties for both wind speed and direction (Newsom et al. 2017), and the uncertainties between two different levels are assumed to be independent. The profiler observations of speed and direction at each level were perturbed by a normally distributed random number with a mean of zero and a standard deviation taken from the ARM product. While this approach could result in unphysical values (i.e., perturbations could create wind speeds less than zero or wind directions greater than 360°), these anomalies naturally resolved themselves when the speed and direction were converted to wind
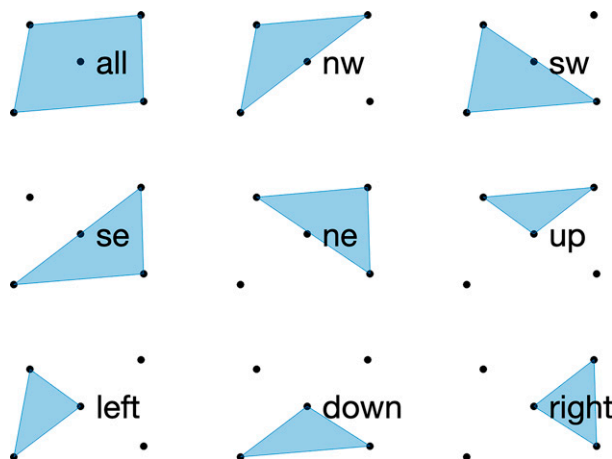

FIG. 2. Schematic of the various polygons that can be defined by the five observation site nodes that comprise the ARM SGP network. The "all" polygon is a quadrilateral that is comprised of the four extended facility observing sites. The four polygons named after compass directions are triangles with an extended facility site at each vertex. The four polygons named after relative directions are triangles with vertices at two extended facilities and one vertex at the central facility.

vector components u and v for implementation in the line-integral calculations. In the present work, the final value for a given parameter and the instrument uncertainty was found by calculating that parameter for 200 separate realizations of perturbed thermodynamic and wind profiles, then taking the mean and standard deviation of those values.

The AERI thermodynamic retrievals and the DLID wind profiles have separate vertical and temporal spacing. AERI profiles are retrieved on a vertical grid with spacing that increases approximately exponentially with height, while the DLID profiles are output on a vertical grid with approximately 26-m vertical spacing that begins 91 m above the surface. After the data were perturbed as outlined above, they were then interpolated onto a common grid to facilitate analysis, with vertical spacing of 50 m and a temporal interval of 15 min. The elevation of the terrain in north-central Oklahoma is not constant and so approximately 100 m of relief is found between the lowest and highest observing facility (as seen in the elevation map in Fig. 1); however, in practice this works out to a slope less than 0.02%. The calculations were made relative to the same heights above ground level at all sites. Calculations are performed on a level-by-level basis, which means that correlations between calculated quantities at adjacent levels are a natural consequence of the correlations present in the input profile instead of an artifact of the calculation technique.

With the arrangement of one central site surrounded by four extended facilities, there are multiple polygons that can be drawn with a site at each vertex (Fig. 2). This includes a quadrilateral with the four extended facilities at each vertex (hereafter called "all"), four triangles with each vertex consisting of an extended facility (called "ne," "se," "sw," and "nw"), and four triangles with one vertex at the central facility

and two vertices at the extended facilities (called "up," "left," "down," and "right"). The triangles composed of extended facility vertices are approximately half the size of the "all" polygon, while the triangles that include the central facility as a vertex are approximately one-quarter that size. If the value for advection or other field quantities is constant across the domain, then the sign and magnitude of the Green's theorem–based method for determining those values will be consistent across the various polygons. In practice, variations will be seen between the different polygons as each represents a different region over which the target variables are being assessed.

4. The meteorology of 8 August 2017

To evaluate the appropriateness and utility of the Green's theorem method to calculate these parameters, both model and observational data over the course of a particular 24-h period are examined. The target day, 8 August 2017, was chosen because it took place during a large field campaign and thus is of interest to a larger research community, but it was also synoptically quiescent and therefore well suited for the analysis of smaller-scale processes. The Land Atmosphere Feedback Experiment (LAFE; Wulfmeyer et al. 2018) was a field campaign during the month of August 2017 devoted to investigating interactions between the atmosphere and the surface, and the regular SGP observations were augmented with additional passive and active remote sensing instrumentation. Project goals included observing profiles of fluxes, evaluating similarity relationships, and characterizing the moisture budget within the experiment domain. Clearly, achieving these objectives depends to some degree on quantifying the advection: observations of changes in water vapor at the SGP Central Facility are a function of local influences on the water vapor content as well as changes due to advection. By using the methods described here to calculate the magnitude of the observed change caused by advection, it is then possible to determine the influence of the local environment on the atmospheric state. This initial analysis is contemporaneous with one of the LAFE intensive operation period (IOP) days to support the analysis of data from this campaign even though none of the additional instrumentation deployed during LAFE was necessary for the results shown here; similar investigations using the routine ARM observations can therefore be carried out as far back as spring 2016 when the extended facility network was developed and Doppler lidars and thermodynamic profilers were deployed at the various facilities (Gustafson et al. 2020).

A broad anticyclone covered much of the central United States (including the SGP domain) on this day so observed changes in the atmospheric state were mostly locally driven. Due to the position of the SGP site relative to the center of the anticyclone located around southeastern Iowa to northeastern Illinois, surface and near-surface winds at the various ARM observing sites were from the east and north as opposed to more southerly or westerly as would be expected; as a result, advective tendencies tended to be cool and dry during the daytime hours rather than the warm and moist advection one would anticipate. A cold front stretching from central Texas east-northeast to Virginia slowly sagged to the southeast on 8 August, eventually stalling out and becoming a stationary front that roughly paralleled the coast of the Gulf of Mexico a few hundred kilometers inland. While the front was well separated from the SGP domain, it nevertheless had a key impact on the conditions in the target area as it meant that the warm, moist air that typically flowed northward from the Gulf into Oklahoma remained well to the south during this period allowing the northerly and easterly flow to dominate. The lack of synoptic forcing coupled with a moist boundary layer and little convective inhibition meant that while there was little large-scale cloudiness driven by dynamics, locally forced shallow cumulus formed throughout the domain during daytime hours. As solar heating diminished in the late afternoon, the cumulus field dissipated and the skies were once again clear by sunset.

5. Algorithm evaluation

a. Results from 8 August 2017

Gridded model output can be used to help evaluate the efficacy of the Green's theorem–based approach as well as identify the impact of changing the size and location of observation sites. Ultimately, quantities like advection and vorticity are defined as combinations of linear derivatives of smoothly varying functions. By applying finite differencing to the fine-scale NWP analysis grids, approximations of the spatial derivatives and gradients of the wind and thermodynamic fields can be calculated and values for advection and other quantities based on the original definitions of these terms can be determined. Such an approach is not unique to this particular study; Bony and Stevens (2019) used model output to evaluate the role that the distribution of dropsondes has on the magnitude and uncertainty of line-integral calculations of divergence. The present study uses analysis output from version 2 of the operational High-Resolution Rapid Refresh (HRRR; Smith et al. 2008; Benjamin et al. 2016) model, which was operational at the time. Finite differences are calculated between the individual 3-km grid cells to arrive at the advection and wind field kinematic parameters for each individual cell, then the value from all of the cells within each of the predefined polygons are averaged together to determine a representative value for that polygon. By applying the Green's theorem method to the same model grids (i.e., by extracting model profiles of temperature, humidity, and wind at each ARM site and calculating the target parameters on that subset of collected profiles) a direct comparison of the efficacy of the Green's theorem method versus the finite difference definition can be made. Should there be substantial agreement between the two methods, then it is possible to state that the Green's theorem method is a reasonable approximation for the derivative-based definition and thus suitable for scientific analysis.

Figure 3 illustrates the results of such an analysis for the 8 August 2017 case. Here, HRRR 0-h analyses are used to calculate time–height cross sections of the derived quantities
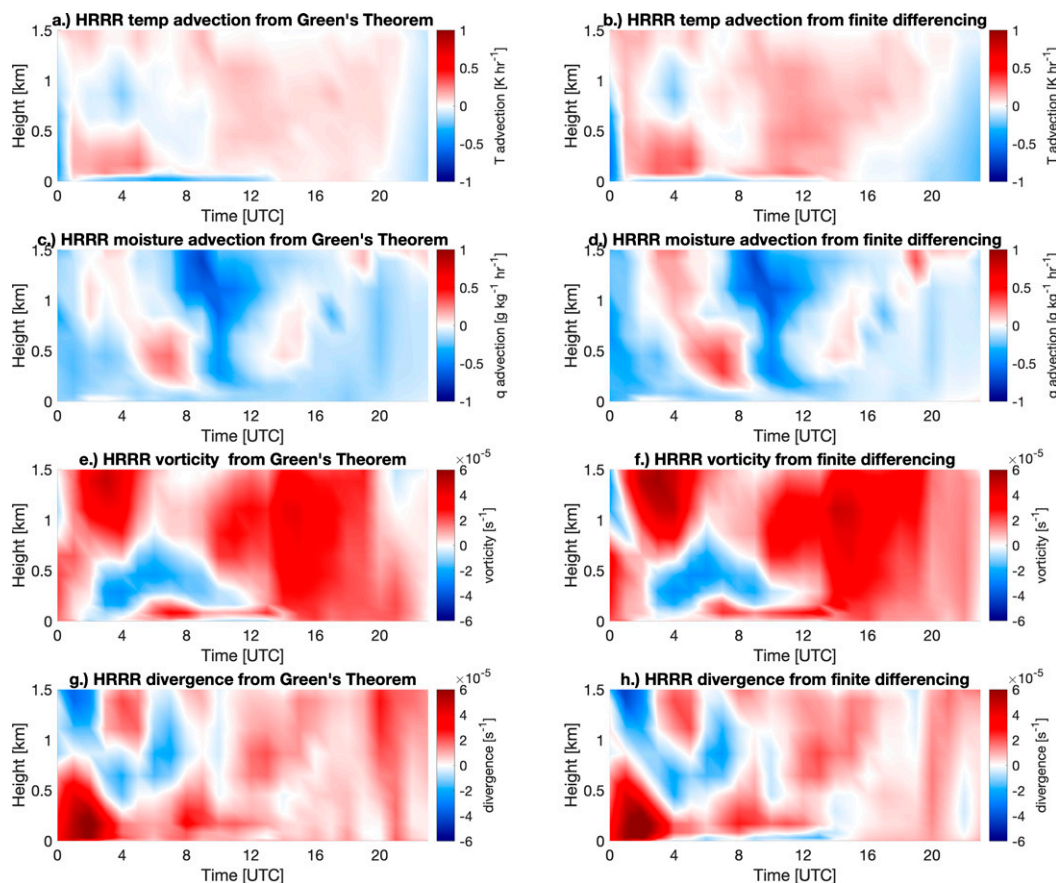
FIG. 3. Time–height cross section for 8 Aug 2017 of various derived parameters as calculated from HRRR model analyses of atmospheric conditions within the "all" polygon. (left) Results obtained by the Green's theorem method of calculating advection from the four individual observation sites and (right) the mean values of the same derived quantities as calculated by finite differences for each model cell within the polygon. Times are in UTC; heights are in km AGL.

using two different methods. The left column uses the Green's theorem–based method described above. Profiles of temperature, mixing ratio, and winds are taken from the locations of the four extended facilities, and the equations from Table 1 are used to calculate the desired parameters. The right column of Fig. 3 displays the mean results from finite differencing calculations of the desired parameters for each cell within the "all" domain. Shearing and stretching deformation are not presented here, but their performance is similar to the other kinematic quantities. Clearly, there is strong qualitative and quantitative agreement between the two methods with every parameter agreeing well in both magnitude and sign; for example, the mean absolute difference between the two temperature advection plots is only 0.06 K h^{-1}. While there are some subtle differences between the two methods, overall confidence is high that the Green's theorem method is a suitable tool for evaluating advection and other derived quantities with a network of vertically profiling observation sites. Similarly, Bony and Stevens (2019) found good quantitative agreement between Green's theorem calculations of divergence (and the associated vertical velocity) and the direct model output.

Another method to assess the utility of the Green's theorem method is to evaluate the variability of the results as calculated for the different polygons that can be made using various combinations of the central and extended facilities. Figure 4 shows the results for the Green's theorem–based moisture advection for each of the nine polygons outlined in Fig. 2. Qualitatively, the nine polygons show good agreement with each other, though it is clear that nonnegligible differences do exist between them. For example, while most of the polygons illustrate moist air advection from 1200 to 1600 UTC between 0.5 and 1 km AGL, three of them ("nw," "ne," and "up") are actually exhibiting strong dry-air advection at those times and heights. Each of those three polygons share one leg in common (the E32 to E41 leg, as seen in Fig. 1, that represents the northern border of the SGP domain) which implies that the mean moisture and/or wind conditions along that leg are well displaced from those along the other legs within the domain. A more extreme example of variability between domains is shown later (see Fig. 6), which illustrates the time–height cross sections of temperature advection for the same period depicted in Fig. 5. Here, it is clear that the sign of the temperature advection for three polygons ("ne,"
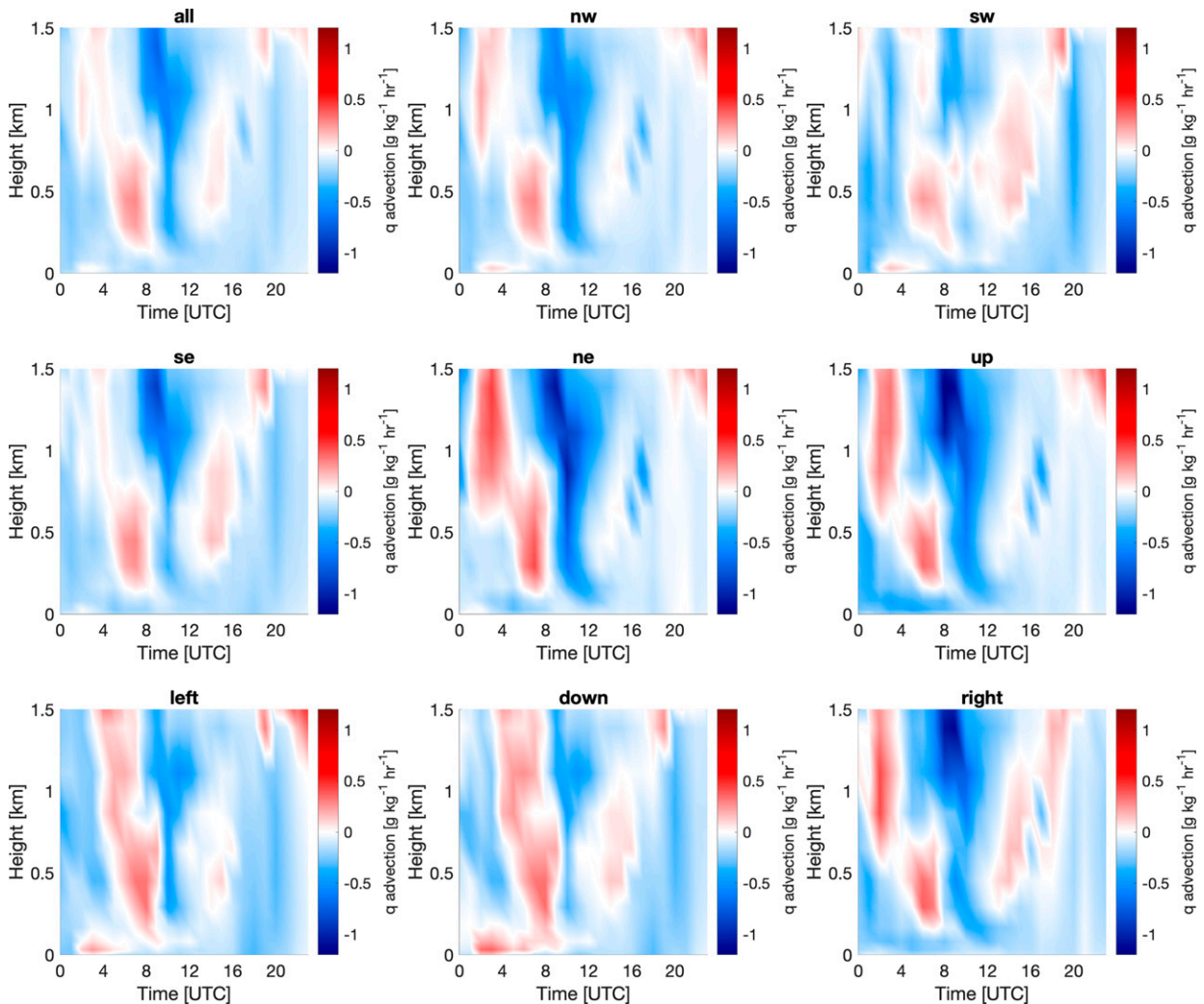
FIG. 4. Time–height cross section of water vapor advection (in g kg^{-1} h^{-1}) calculated from the HRRR analyses using the Green's theorem method for 8 Aug 2017 over each of the nine different polygons defined in Fig. 2. Times are in UTC; heights are in km AGL. (top left) "All" is equivalent to Fig. 3c.

"right," and "up") is reversed compared to the other six polygons. As seen before with the anomalous water vapor cross sections, these outlying polygons have some commonality: they all have a common point in E41. Similar behavior (not shown) was also seen when comparing the finite differencing results from these polygons to the others. While it is challenging to definitively state that a given calculation is truly representative of a heterogeneous environment, it is true that adjacent polygons are representing different locations and differences between the calculated values from one polygon to the next are due, in part, to physical changes in the environment and not just an artifact of how the polygons are defined.

To quantify that last point, the HRRR analyses can be used to determine the impact of polygon definition on the calculated values. In this case, the locations of the observing sites can be displaced via a Monte Carlo approach to see how slightly modified polygon shapes can impact the calculated values. The locations of each of the four observing sites in the

"all" polygon were displaced in both the x and y directions by a random value chosen from a normal distribution with a standard deviation of 10 km, which is approximately 20% of the spacing between sites, to discern how the calculated results would change if ARM had chosen slightly different locations for its sites. A total of 10 000 trials were carried out and the mean and standard deviation of the target quantities were calculated at every time and height during the evaluation period. The mean (not shown) corresponds nearly identically with the unperturbed plots displayed in the left column of Fig. 3. The standard deviation can serve as a measure of the variability of the measured parameter as the domain changes, which in turn helps quantify the impact of site representativeness. This is not a true uncertainty or error, since even a perfect measurement will experience variability when the measurement domain changes in a nonuniform field. Still, it is instructive to assess how much the measured quantities change with the changing domain, and the standard deviations
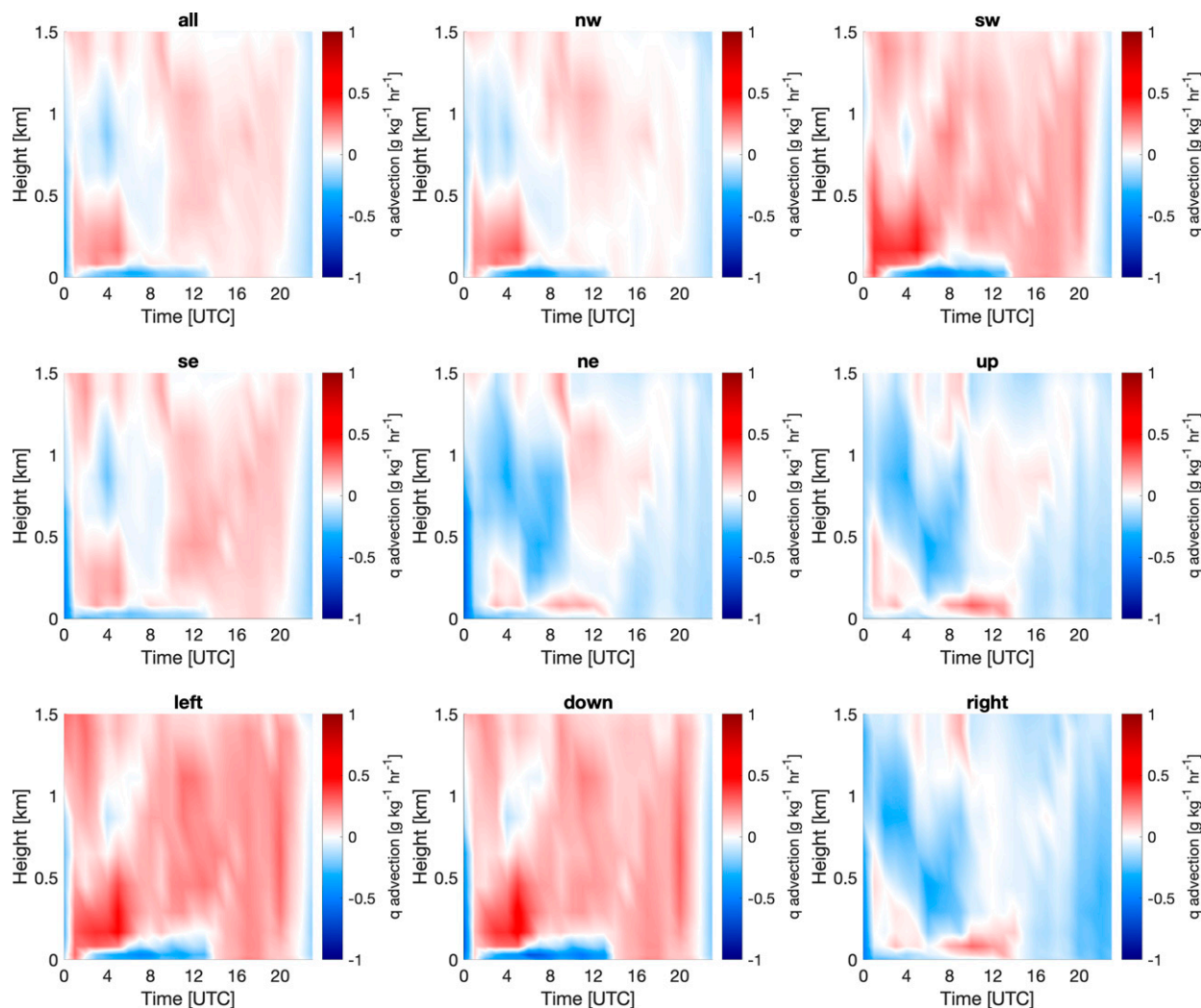
FIG. 5. As in Fig. 4, but for temperature (in K h^{-1}).

are shown in Fig. 6 for temperature advection (top panel) and vorticity (bottom panel) provide one estimate of the sampling error associated with the location of the vertices. For most times and heights, these sampling errors amount to approximately a 20% envelope of variability around the mean value for both the temperature advection (which includes both temperature and wind information) and the vorticity (which only relies on winds). However, there are instances in which these sampling errors can increase to over 200% as the domain expands to include nearby locations with substantially different conditions, or to even larger percentages when the mean value approaches zero and the resulting relative error requires dividing by a near-zero number.

b. Multiday statistical analysis

While it is instructive to look at these single-day analyses to gain an overview on the behavior of the Green's theorem method, additional insight into the implementation of this method can be gained by evaluating statistical correlations

between the Green's theorem and finite differencing methods over a longer period of time. In this section, the HRRR analysis dataset is expanded to include several adjacent days (1–9 August 2017) to compare the two methods and provide more insight into their relationship with one another. The lowest 14 model levels (from the surface to approximately 3 km) from analyses generated every three hours were used in this section. Only the 0000 UTC data from 5 August 2017 were available for this analysis, and significant storms during the 0000 UTC run on 4 August 2017 caused significant cold pooling and strong deviations between the two methods, so those values were excluded so that more quiescent conditions were present. This is not considered to be a significant limitation as AERIs are unable to operate during precipitation anyway, and therefore, these conditions are more representative of real-world observations. As before, the Green's theorem method was applied to the HRRR data by extracting vertical thermodynamic and kinematic profiles from the grid point nearest to the vertices of the desired polygon, then compared
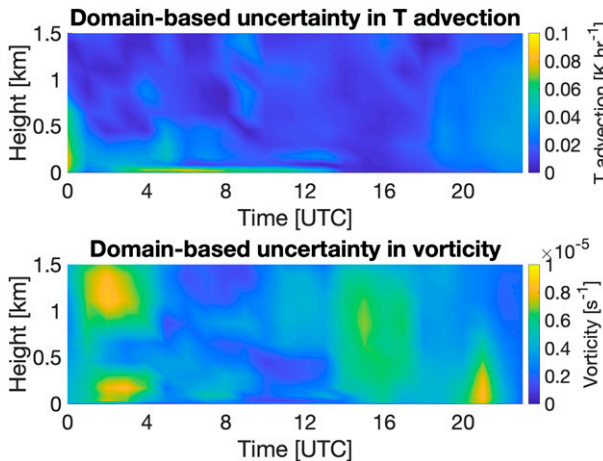
FIG. 6. Time–height cross sections of the domain-based uncertainty in the calculated (top) temperature advection (in K h^{-1}) and (bottom) vorticity (in s^{-1}).

to the mean values calculated from finite differencing between all grid cells within that polygon.

When using the Green's theorem method, it is assumed that the meteorological conditions along the sides of the polygon are linearly and monotonically varying such that the mean values of the endpoints of a given side are representative of the conditions along the side. Michael (1994) notes that one way to ensure that this assumption is valid is to increase the number of observation sites so that the linear line-integral approximation applied here behaves more like a true line integral. The HRRR output facilitates an analysis of the impact of additional observation sites. Here, a total of 8, 16, and 32 sites are evaluated relative to the "all" polygon with 4 sites by simply placing new observation points halfway along each polygon side, then halfway between those points, and halfway again. The calculations are then compared to the finite differencing results. Since this process preserves the location and shape of the polygon, the finite differencing results are identical in each of these tests. Figure 7 is a scatterplot of temperature advection for the 4, 8, 16, and 32 point calculations. It is clear that doubling the number of observation points to eight shows a slight improvement relative to the original four points, but any additional increase in observation density has little impact. This is consistent with the findings of Michael (1994), which showed that this truncation error had very little impact for polygons with five points or more, though different from Bony and Stevens (2019), which found that doubling or quadrupling the number of points continued to decrease the uncertainty of their divergence calculations. Figures 8 and 9 show similar plots for water vapor and vorticity, respectively. As before, the additional benefit beyond the first doubling of observation density is weak. A key takeaway
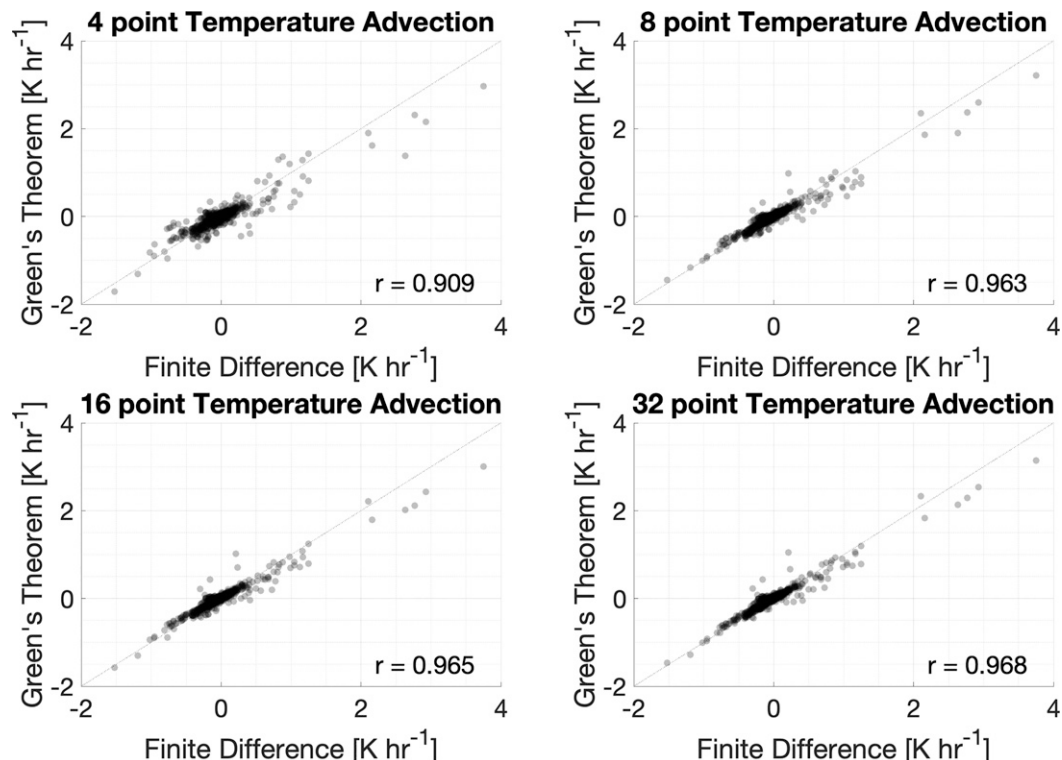

FIG. 7. Scatterplot of the calculated temperature advection (in K h^{-1}) for the finite difference (*x* axis) and Green's theorem (*y* axis) methods for the multiple-day model dataset, evaluated over the SGP domain but with different numbers of simulated observing points. The correlation coefficient is displayed in the lower-right corner of each panel. The 1:1 line is also plotted.
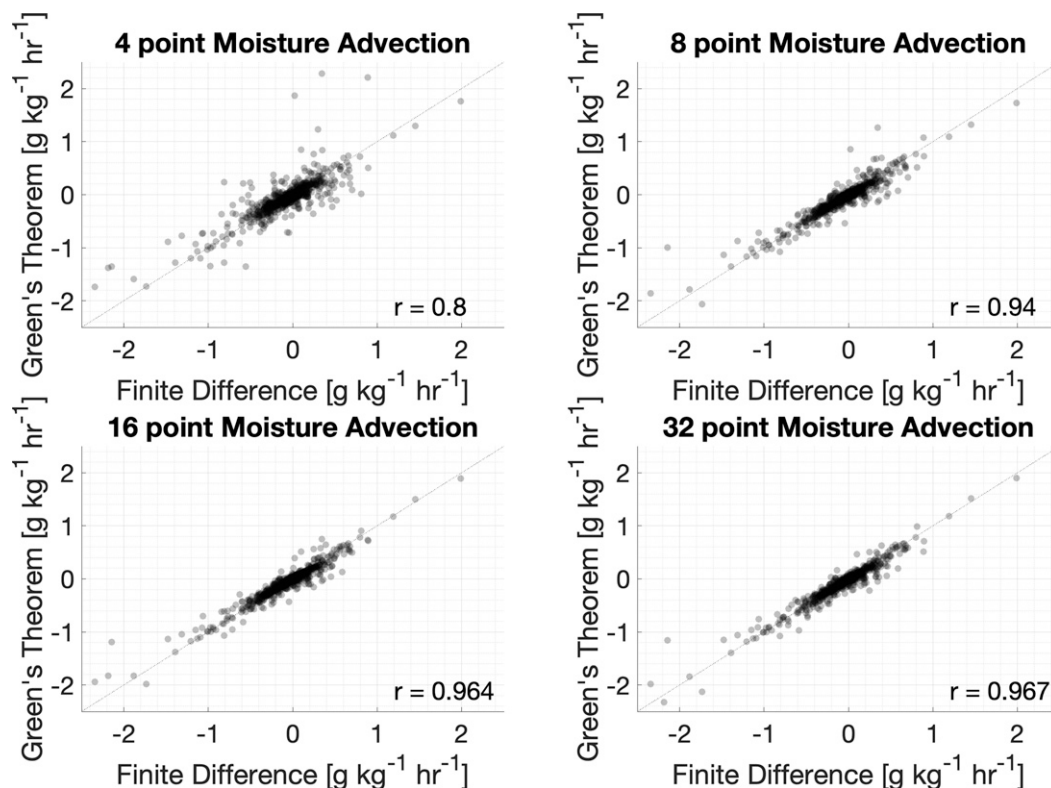
FIG. 8. As in Fig. 7, but for moisture advection (in g kg^{-1} h^{-1}).

from this analysis is that even when the fewest number of points are used, the correlation between the finite differencing and Green's theorem methods is strong and there appears to be little influence by the alongside variability. The Green's theorem method also implicitly assumes that the air flowing through the domain is unaffected by latent or sensible heat fluxes to or from the surface as such exchanges could not be accounted for by only evaluating conditions on the periphery of the domain. However, the strong correlation between the two methods of observing the target quantities, especially for the 32-point case which has very little linear approximation error, implies that the impact of these exchanges is small for the cases evaluated here.

This dataset also provides the opportunity to evaluate the impact of domain size on the relationship between the finite differencing and Green's theorem results. To evaluate this, the locations of the four observation sites that comprise the "all" polygon were displaced inward and outward in both latitude and longitude in 0.1° increments from −0.2° to 2.0° away from the original coordinates. This resulted in 23 domains that ranged from approximately 0.1 times to over 50 times the area of the original domain. Once again, the advection, vorticity, and other parameters were calculated for each domain as described above. To help facilitate understanding, a characteristic domain length was calculated for each domain which is simply the square root of the domain area, and Fig. 10 illustrates the correlation between the two methods as a function of this domain length. The SGP network has a domain length

of approximately 70 km, which is depicted with a vertical dashed line. After an initial ramp-up, all quantities tend to have worse correlations with increasing area size, with several quantities exhibiting rapid drop-offs at 120 km and beyond. In fact, the existing spacing of the SGP network appears to be well suited to making these kinds of measurements as the correlations for that domain are among the highest for any domain size.

The HRRR analyses can also be used to inform the degree to which the domain size can impact the uncertainties of the observation. Here, Monte Carlo sampling can assess the impact of instrument uncertainty as a function of domain size. Whereas the previous analysis investigated how slightly different placing of the existing sites could impact the observed values, here the "all" polygon is expanded and contracted to encompass a range of areas that encompasses over two orders of magnitude. For small domains, uncertainties in the thermodynamic or wind observations will have a more substantial impact than they will for large domains. For example, a 0.5-K error in temperature will cause a much greater impact when the domain is small and the conditions at the polygon vertices are similar than when the domain is large and the values at the four corners differ significantly. To test this, the modeled profiles are perturbed by random values with a mean of zero and a standard deviation of 0.6 K, 0.5 g kg^{-1}, and 0.5 m s^{-1} for the temperature, mixing ratio, and wind speed, respectively, values that are typical for the observed uncertainty at 1 km AGL (Turner and Löhnert 2014). The advection was
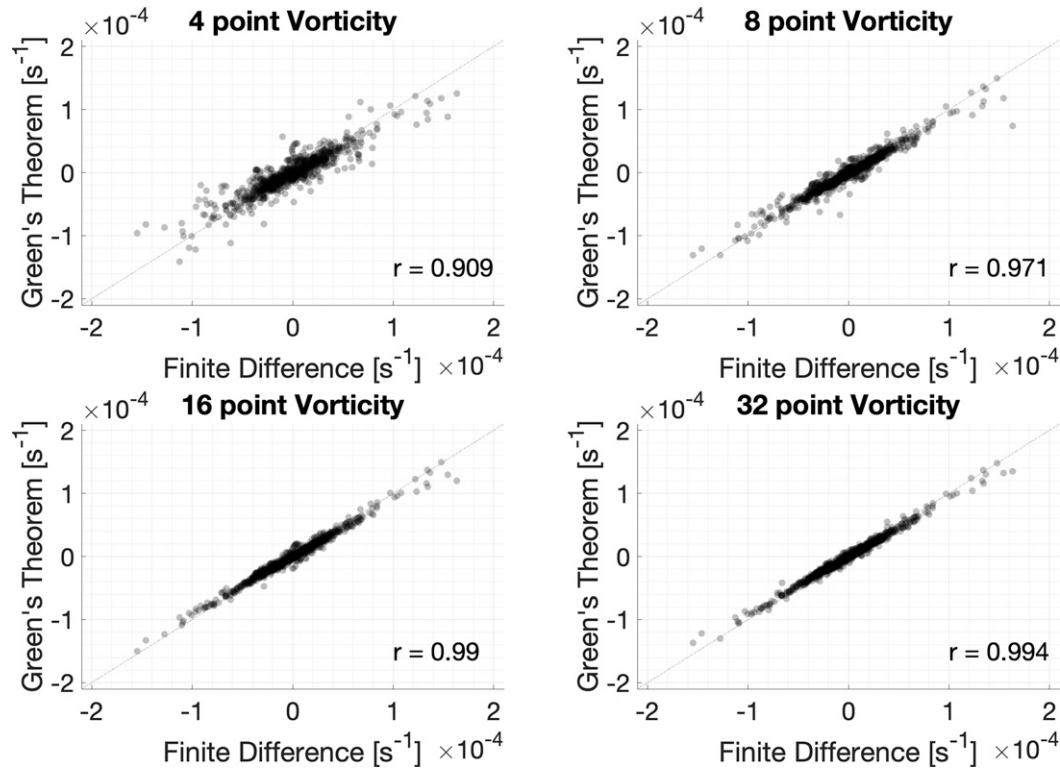
FIG. 9. As in Fig. 7, but for vorticity (in s^{-1}).

then calculated using the Green's theorem method using these perturbed values on domains that were adjusted in the same manner as they were for Fig. 10 above. In addition, sampling uncertainty is assessed by rotating each polygon around the SGP central facility (C1 in Fig. 1) in increments of 15° and finding the standard deviation of the mean advection values
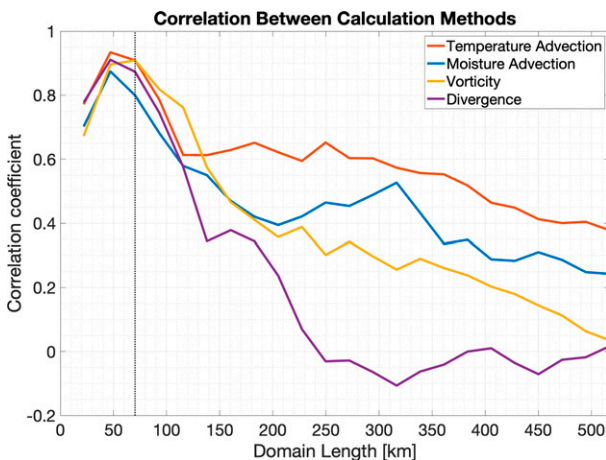

FIG. 10. Correlation between the finite difference and Green's theorem calculations of advection, vorticity, and divergence, as a function of domain length (in km, representing the square root of the domain area) for the multiday model dataset. The dashed vertical line at approximately 70 km represents the domain length of the SGP network.

for each orientation. A total of 50 trials were carried out at four different model levels for each of 24 different orientations of 23 different polygons at 3-h intervals on the 14 lowest levels of the model. Results showed that sampling uncertainty was typically one order of magnitude less than the instrument uncertainty regardless of domain size. The total (instrument plus sampling) uncertainty is shown in Figs. 11 and 12 for temperature and water vapor mixing ratio, respectively. Since the height above ground for a given model level varies from one point to the next, the height values given for each subpanel are approximate heights evaluated at the grid point nearest to the SGP central facility. It is readily apparent that the absolute uncertainty decreases with increasing domain size, as expected; Bony and Stevens (2019) found similar results when calculating divergence uncertainty on different domain sizes. Uncertainties are also generally larger during the nighttime hours than during the day, due to faster winds at night and a greater magnitude for the advection.

Since the absolute uncertainty decreases with increasing domain size, the temptation may be to space observing sites as far from each other as feasible to minimize the impact of the instrument uncertainty on the calculated values. However, the magnitude of the calculated parameters goes to zero as the domain gets larger. As noted in Table 1, regardless of the parameter being sought, all values are determined by first calculating a sum then dividing by the area. Even though placing observation sites far apart likely results in greater differences in meteorological conditions between the sites (and thus, small-scale variability between the sites would not be captured
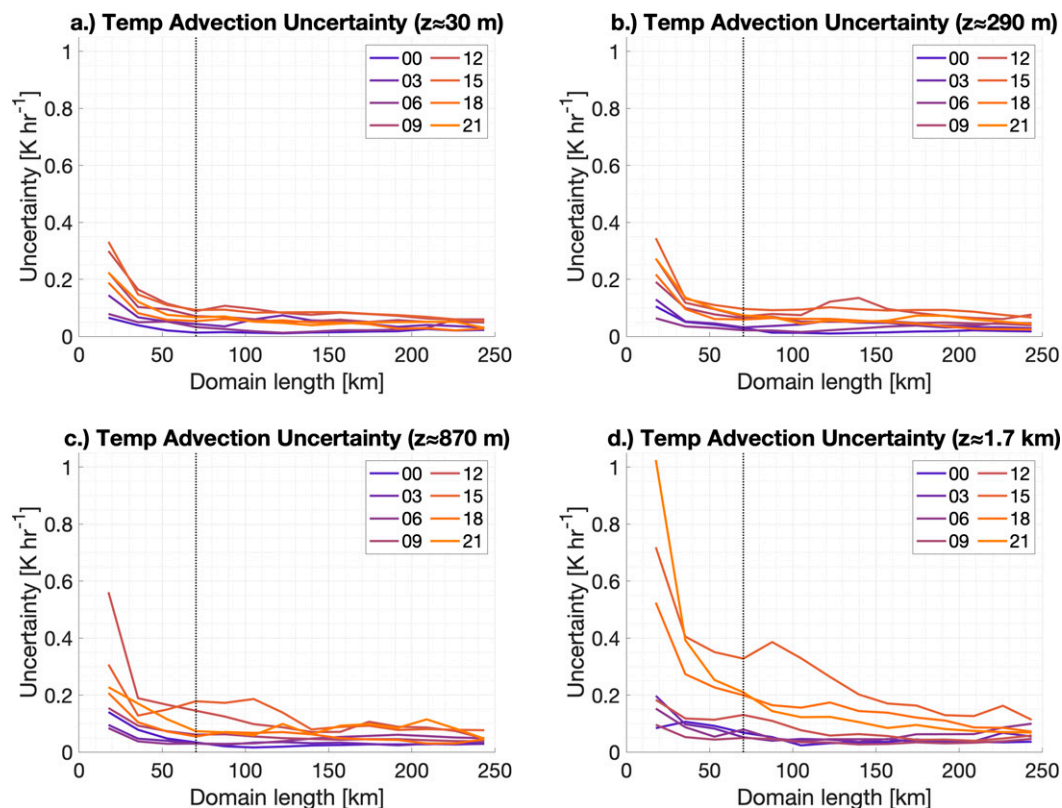
FIG. 11. Theoretical uncertainty in temperature advection (in K h^{-1}) as a function of domain length for four different heights above ground level. Colors represent time of day (in UTC).

in the advection calculation), the increase in area far surpasses these differences and the magnitude of the advective or kinematic parameter goes to zero. The spacing of the SGP sites (marked with the dashed black vertical line in Figs. 11 and 12) is well suited for these calculations: the sites are far enough apart that uncertainty is much less than it would be if the sites were even a few kilometers closer together, but not so far apart that the targeted observations are too close to zero to be useful. This existing spatial scale matches well with current-generation climate model resolution, meaning that these calculations can be used to assist in evaluating similar parameters in climate model output.

6. Observed results

Results from the AERI/DLID profiler network for the "all" polygon are shown in Fig. 13 along with their associated uncertainties due to instrument error. These values were calculated by perturbing the temperature, moisture, and wind input profiles as described in section 3, conducting 200 Monte Carlo trials, and taking the mean of those trials to obtain the desired quantity and the standard deviation to find its uncertainty. The times, heights, and color bar ranges here are the same as those in Fig. 3, so direct comparisons of the modeled and observed values are possible. At this time of year, local time is UTC − 5 h, and sunset and sunrise for 8 August 2017

were at 0128 and 1142 UTC, respectively. Overall, there is good qualitative agreement between the temperature advection observations and its modeled equivalent: for example, the mostly warm air advection in the lowest kilometer of the atmosphere that can be found before 1800 UTC switches sign and becomes cold air advection in the late afternoon in both the modeled and observed advection. The moisture advection is somewhat more challenging to interpret: while both model and observations indicate the PBL is drying due to negative moisture advection throughout the observed period, the observations tend toward more moist air advection during the morning and early afternoon than is seen in the modeled values. The instrument uncertainties for both temperature and water vapor advection are larger at night than they are during the day, as was seen earlier in the synthetic study (Figs. 11 and 12). The wind-only parameters of vorticity and divergence show better agreement between observations and the model during the evening and overnight hours than the daytime, which is to be expected when flows are more steady state and fewer transient phenomena are occurring at time scales that are too fine to be resolved by an hourly model.

The observations illustrate some of the relative advantages and disadvantages of the two instruments used here, as well as some of the structures and phenomena that are unable to be captured by the model's hourly output. The active observations of the DLID enable it to observe more structure in the
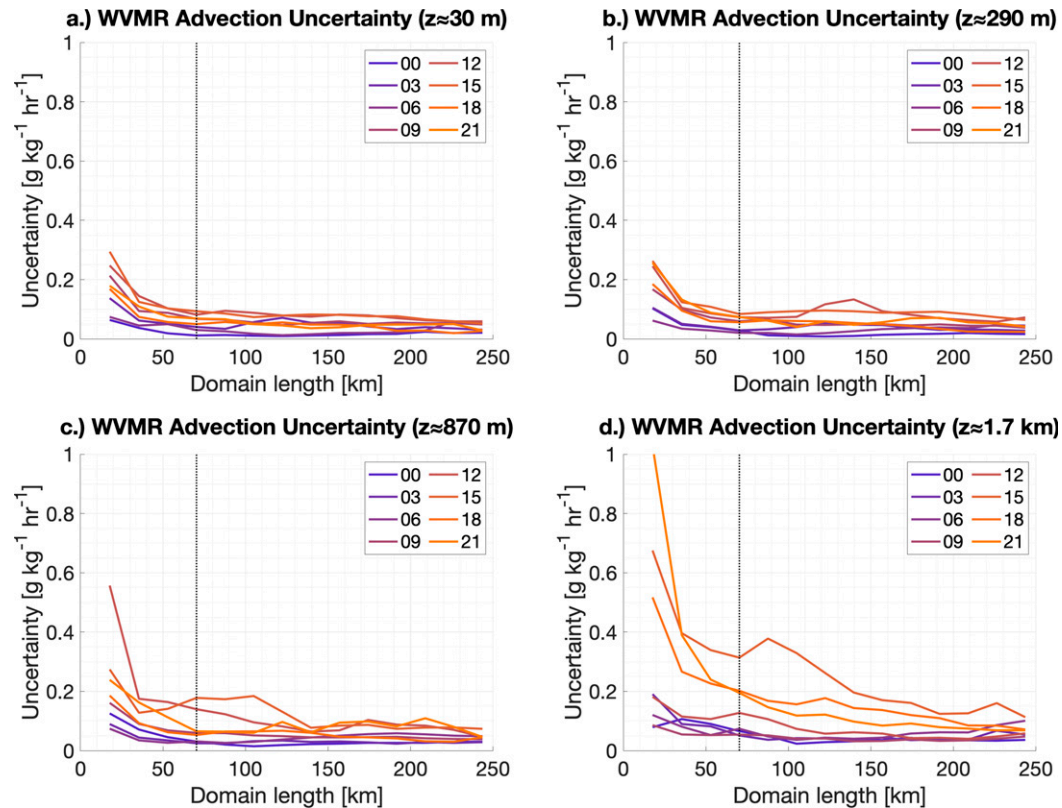
FIG. 12. As in Fig. 13, but for water vapor mixing ratio (in g kg^{-1} h^{-1}).

vertical profiles than is possible with the retrieved thermodynamic profiles from the passively observed AERI spectra. Furthermore, more degrees of freedom of the signal (i.e., information content) are present in the TROPoe temperature retrievals than in the water vapor retrievals. Therefore, the water vapor shows more smearing in the vertical structure than the temperature, while both have less structure than the winds do. However, the AERI is able to produce vertically continuous profiles throughout the depth of the lower troposphere while the DLID is limited to depths where sufficient backscatter can be found; Fig. 14 shows that heights with usable signal are both highly variable with time and can contain vertical gaps. Since multiple DLIDs are required for a calculation, the calculated results are limited to the heights attained by the DLID with the worst performance at a given time. Note that the active approach to remote sensing results in a blind zone near the surface of approximately 100 m as the instrument requires a finite time to transition from emitting to receiving. Unlike the advection observations, the kinematic observations have the greatest uncertainty during the daytime hours. This is because boundary layer turbulence forced by daytime heating increases the likelihood that the wind violates the assumption that horizontal flow through the conical scan volume is constant at a given height (Newsom et al. 2017). Since vorticity and divergence are both comprised of different combinations of linear differences of u and v winds, the uncertainties of those two parameters are very similar,

though the uncertainty in the divergence is slightly larger than the uncertainty in the vorticity.

Differences between the modeled and observed quantities are not necessarily due to limitations of the instruments or the observing method, as the model is not a perfect representation of the atmospheric state at a given place and time, especially at the scale of these observing systems. Rather, these model–observation comparisons are presented here in order to qualitatively illustrate how the same method can produce similar results when applied to two different data sources. While there are concerns about the structure and vertical extent of the observations, they clearly have some advantages over the model analysis, including finer vertical and temporal sampling and a likely better representation of the actual state of the PBL. Although work has been done to illustrate the benefits of assimilating AERI observations into numerical weather models (e.g., Lewis et al. 2020; Coniglio et al. 2019; Hu et al. 2019; Degelia et al. 2020), there has been less of a focus on evaluating model performance with these kinds of observations and it is currently difficult to ascertain how model error may be affecting these intercomparisons. A clear example of structures resolved by the rapid sampling of the observations can be seen in the afternoon hours of the divergence cross section, where strong coherent divergence and convergence structures alternate on roughly an hourly time scale. Since this represents the mean divergence over an area that is hundreds of square kilometers in size, these are not
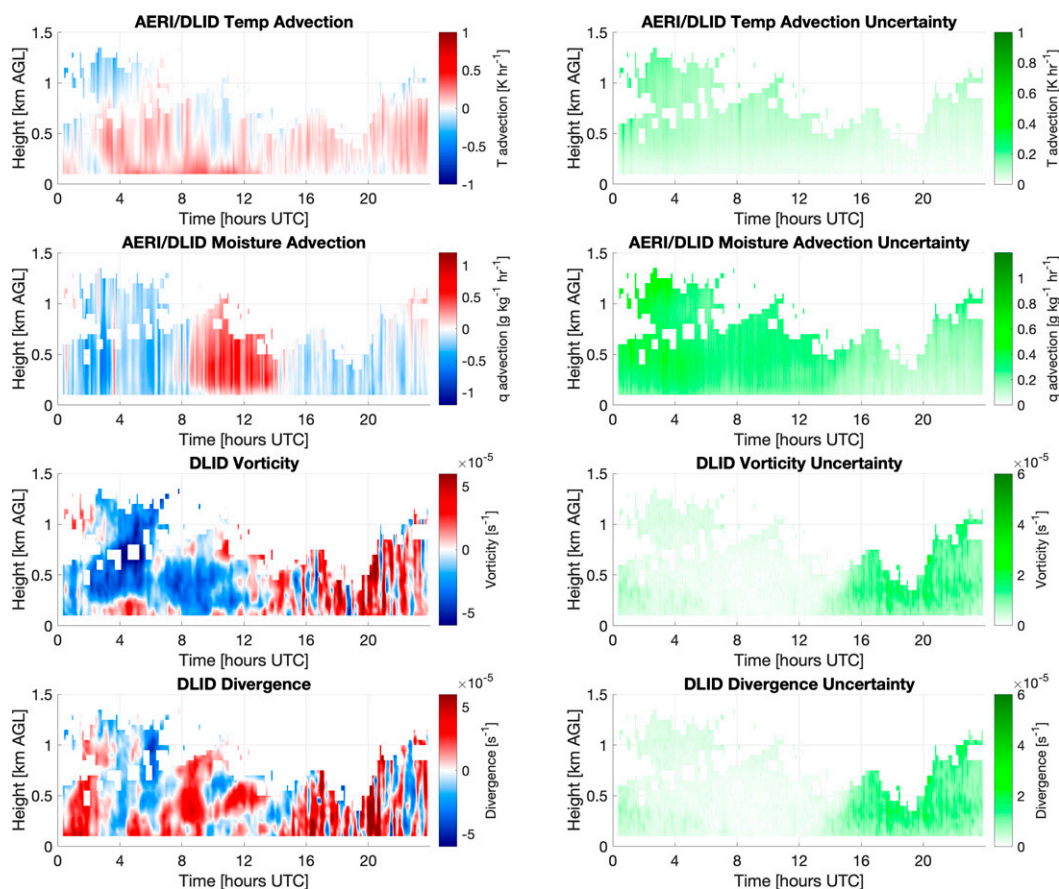
FIG. 13. Time–height cross sections of DLID (and AERI, where appropriate) observations of advection, vorticity, and divergence for the "all" polygon along with uncertainties of the same as derived from the uncertainty of the observing instruments.

plumes associated with individual convective clouds but instead represent a phenomenon occurring on a larger scale. Resolving and investigating phenomena like these are a major reason why the network-based approach to calculating advection and kinematic parameters is useful for increasing our understanding of atmospheric processes.

As was previously done with the model output, it is important to assess how the choice of polygon impacts the parameters calculated from observations. Figure 14 illustrates the temperature advection from each of the nine polygons. There are two key characteristics in this figure that are worth noting: first, since the DLIDs have varying vertical extents at each location due to the local presence of scatterers, the height of the observed products varies among each of the polygons. Second, the reversal in sign for three polygons that was evident in the model results ("ne," "up," and "right" in Fig. 5) is also present here. This lends credence to the idea that such a phenomenon is a legitimate signal rather than an artifact of how the data are being observed and the target parameters are being calculated, although this is somewhat tempered by deeper layers of positive advection in the observations as compared to the model for those polygons. Again, though, perfect correspondence between the observed and modeled values is not anticipated.

7. Summary and conclusions

Kinematic wind parameters, temperature advection, and moisture advection are fundamentally important characteristics of the environment that have a profound impact on the evolution of the atmospheric state on a wide spectrum of spatial and temporal scales, but can be challenging to observe directly from real-world observations that are not deployed on a uniform grid. Techniques have been developed to use the vector calculus–based Green's theorem approach to approximate the advection, vorticity, divergence, and deformation over a finite domain directly from a network of observations. The present work applies such methods to the continuous observations of temperature, moisture, and winds from the ground-based profiling network at the ARM Southern Great Plains site in Oklahoma.

A multistep approach was used to illustrate the effectiveness of these methods beginning with a single day for analysis. Hourly analyses from the operational HRRR model were used to compare finite difference calculations (for which advective and kinematic quantities can be calculated directly from their original definitions) to the Green's theorem method. Strong qualitative agreement between the two methods was found so long as one assumes that the mean
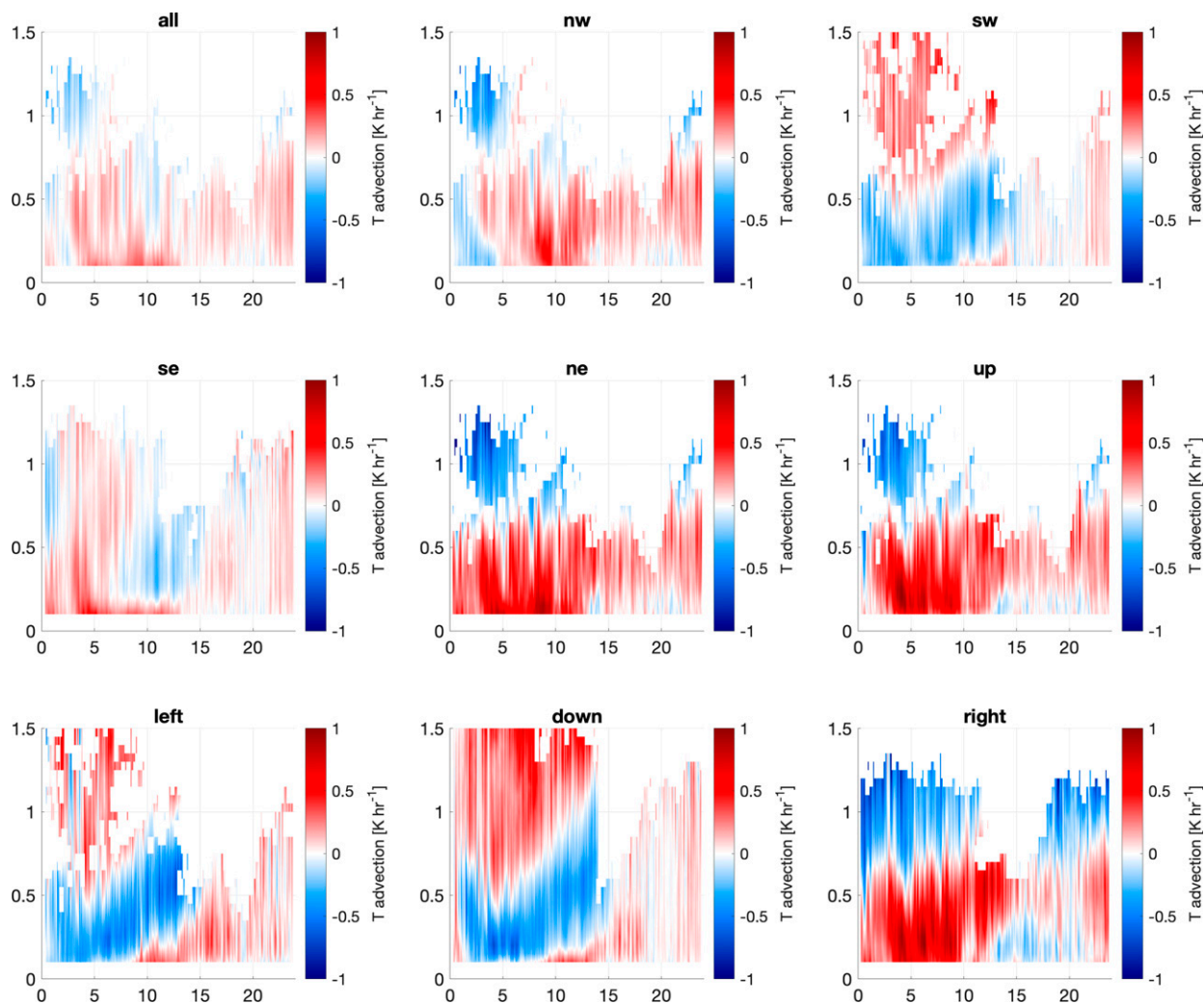
FIG. 14. Time–height cross sections of AERI + DLID–observed temperature advection (in K h^{-1}) for each of the nine polygons created from the nodes in the ARM SGP observing network.

advection through the evaluation polygon is the same as the mean of the advection from each model grid cell within that area. The variability in calculated quantities among different polygons was demonstrated, and while it was found that magnitudes and signs of the target parameters can vary from one polygon to the next, both methods largely agreed for a particular polygon. Since the polygons encompass different areas with different conditions along their edges, changes between polygons are not necessarily a limitation of the observing method, but instead one measure of the sampling error of the method. The role of site selection and its impact on the calculated parameters was also explored through a Monte Carlo simulation in which the locations of the observing sites were randomly displaced. It was found that changing the locations of the profiling nodes has an impact on the calculated values that, while usually small, can occasionally rise to be greater than the magnitude of the calculation itself, especially as the calculation changes sign. Clearly, great care must be taken during the deployment of an observing network to ensure

that the observation site is representative of the larger area if accurate low-level advection and derived wind field observations are desired, as a nonrepresentative site can have a substantial impact on the accuracy of the calculations through the introduction of specious values for the vertex observations.

Additional testing to determine how the number of sites and the size of the domain can influence the observations and their uncertainties was also undertaken. In this case, over a week's worth of analyses taken every 3 h from the HRRR were used to create a dataset representative of a longer period of time. As before, the gridded HRRR output was used to calculate values using both the finite differencing and Green's theorem methods. For the SGP domain, both methods had strong correlations for all targeted parameters regardless of the number of observation points. The strongest correlations were found for domains between 50 and 70 km on a side (a distance that is representative of the SGP domain), and decreased with increasing size. Uncertainties were at a maximum for the smallest domain evaluated, and were higher

during the afternoon and at higher altitudes than for other times and heights. Sampling errors were found to be approximately an order of magnitude smaller than the uncertainty in the derived quantity caused by instrument uncertainty.

Following these synthetic tests, the Green's theorem method was applied to the real-world remotely sensed profiles of temperature, mixing ratio, and winds available from the ARM SGP observing network to create time–height cross sections of the advective and kinematic parameters. The observations qualitatively agreed with the model results illustrated earlier, though kinematic quantities showed better agreement during the nighttime hours than during the day. Instrument uncertainties for the observations were also calculated using a Monte Carlo approach, demonstrating that the uncertainties are usually on the order of 10%–20% of the absolute magnitude of the parent quantity and are larger at night for the thermodynamic quantities but larger during the day for the kinematic ones.

Although a single day of observations is presented here as a proof of concept, it is important to note that the ARM SGP profiling network has been operating nearly continuously since 2016 with only occasional downtimes for maintenance and instrument replacement. Therefore, a large dataset exists that can be used to calculate the advective and kinematic values over a long period of time. The SGP network is well suited for making these calculations from observations, and this work demonstrated this network is well sized for such a purpose. For the cases investigated here, the correlation between the Green's theorem method and values calculated from finite differencing is near its maximum when calculated over a domain the same size as the extant network. Furthermore, the uncertainties are smaller than they are for larger domains, yet the domain is not so large that the desired parameters tend toward zero. While it may be that the ideal domain size varies depending on synoptic flow and other conditions, based on the results found here it is recommended that future deployments of observing networks attempt to place the sites approximately 60–70 km apart to maximize the utility of these observations for advective and kinematic field calculations.

One of the primary objectives of LAFE is to use observations to close the water vapor and temperature budgets over the SGP site (Wulfmeyer et al. 2018), and the work presented here can help quantify components of the budgets that have historically been difficult to measure. With a multiyear dataset available, the approach outlined here can be used to evaluate seasonal tendencies in advection, the dependence of the magnitude of the advection based upon wind speed and direction, and an investigation on how the annual cycle of crop growth and land cover changes can impact the moisture advection through the SGP domain. Future work will also assess characteristic changes in advection throughout the diurnal cycle. The impacts of specific phenomena on the temperature and moisture budgets over the region can also be addressed using the procedures outlined here.

Finally, while this approach was demonstrated for ground-based profiling systems, it need not be limited to just those observations. As noted earlier, vorticity and divergence have been calculated from dropsonde profiles. Furthermore, collocated observations of thermodynamic values with atmospheric motion vectors from satellites could be used to produce similar values over a much larger array of polygons. With future generations of satellites promising hyperspectral profiling from geostationary orbit, it would be possible to generate near-continuous assessments of upper level divergence and advection on a continental scale in near–real time.

Data availability statement. All data used in this study were downloaded from the Atmospheric Radiation Measurement (ARM) archive at www.arm.gov. The exception to this is the digital elevation data used in Fig. 1, which were obtained from the U.S. Geological Survey (USGS) National Elevation Dataset (NED) via the National Map.

REFERENCES

Benjamin, S. G., and Coauthors, 2016: A North American hourly assimilation and model forecast cycle: The Rapid Refresh. *Mon. Wea. Rev.*, **144**, 1669–1694, https://doi.org/10.1175/MWR-D-15-0242.1.

Blumberg, W. G., D. D. Turner, S. M. Cavallo, J. Gao, J. Basara, and A. Shapiro, 2019: An analysis of the processes affecting rapid near-surface water vapor increases during the afternoon to evening transition in Oklahoma. *J. Appl. Meteor. Climatol.*, **58**, 2217–2234, https://doi.org/10.1175/JAMC-D-19-0062.1.

Bony, S., and B. Stevens, 2019: Measuring area-averaged vertical motions with dropsondes. *J. Atmos. Sci.*, **76**, 767–783, https://doi.org/10.1175/JAS-D-18-0141.1.

Bourassa, M. A., and K. M. Ford, 2010: Uncertainty in scatterometer-derived vorticity. *J. Atmos. Oceanic Technol.*, **27**, 594–603, https://doi.org/10.1175/2009JTECHO689.1.

Carlson, C. A., and G. S. Forbes, 1989: A case study using kinematic quantities derived from a triangle of VHF Doppler wind profilers. *J. Atmos. Oceanic Technol.*, **6**, 769–778, https://doi.org/10.1175/1520-0426(1989)006<0769:ACSUKQ>2.0.CO;2.

Clough, S. A., M. W. Shepard, E. J. Mlawer, J. S. Delamere, M. J. Iacono, K. Cady-Pereira, S. Boukabara, and P. D. Brown, 2005: Atmospheric radiative transfer modeling: A summary of the AER codes. *J. Quant. Spectrosc. Radiat. Transfer*, **91**, 233–244, https://doi.org/10.1016/j.jqsrt.2004.05.058.

Coniglio, M. C., G. S. Romine, D. D. Turner, and R. D. Torn, 2019: Impacts of targeted AERI and Doppler lidar wind retrievals on short-term forecasts of the initiation and early evolution of thunderstorms. *Mon. Wea. Rev.*, **147**, 1149–1170, https://doi.org/10.1175/MWR-D-18-0351.1.

Davies-Jones, R., 1993: Useful formulas for computing divergence, vorticity, and their errors from three or more stations. *Mon. Wea. Rev.*, **121**, 713–725, https://doi.org/10.1175/1520-0493(1993)121<0713:UFFCDV>2.0.CO;2.

Degelia, S. K., X. Wang, D. J. Stensrud, and D. D. Turner, 2020: Systematic evaluation of the impact of assimilating a network

of ground-based remote sensing profilers for forecasts of nocturnal convection initiation during PECAN. *Mon. Wea. Rev.*, **148**, 4703–4728, https://doi.org/10.1175/MWR-D-20-0118.1.

Gustafson, W. I., Jr., and Coauthors, 2020: The Large-Eddy Simulation (LES) Atmospheric Radiation Measurement (ARM) Symbiotic Simulation and Observation (LASSO) activity for continental shallow convection. *Bull. Amer. Meteor. Soc.*, **101**, E462–E479, https://doi.org/10.1175/BAMS-D-19-0065.1.

Helms, C. E., and R. E. Hart, 2012: The evolution of dropsonde-derived vorticity in developing and non-developing tropical convective systems. *30th Conf. on Hurricanes and Tropical Meteorology*, Ponte Vedra, FL, Amer. Meteor. Soc., 10A.2, https://ams.confex.com/ams/30Hurricane/webprogram/Paper205957.html.

——, and ——, 2013: A polygon-based line-integral method for calculating vorticity, divergence, and deformation from non-uniform observations. *J. Appl. Meteor. Climatol.*, **52**, 1511–1521, https://doi.org/10.1175/JAMC-D-12-0248.1.

Hu, J., N. Yussouf, D. D. Turner, T. A. Jones, and X. Wang, 2019: Impact of ground-based remote sensing boundary layer observations on short-term probabilistic forecasts of a tornadic supercell event. *Wea. Forecasting*, **34**, 1453–1476, https://doi.org/10.1175/WAF-D-18-0200.1.

Knuteson, R. O., and Coauthors, 2004a: Atmospheric Emitted Radiance Interferometer. Part I: Instrument design. *J. Atmos. Oceanic Technol.*, **21**, 1763–1776, https://doi.org/10.1175/JTECH-1662.1.

——, and Coauthors, 2004b: Atmospheric Emitted Radiance Interferometer. Part II: Instrument performance. *J. Atmos. Oceanic Technol.*, **21**, 1777–1789, https://doi.org/10.1175/JTECH-1663.1.

Lewis, W. E., T. J. Wagner, J. A. Otkin, and T. A. Jones, 2020: Impact of AERI temperature and moisture retrievals on the simulation of a central plains severe convective weather event. *Atmosphere*, **11**, 729, https://doi.org/10.3390/atmos11070729.

Michael, P., 1994: Estimating advective tendencies from field measurements. *Mon. Wea. Rev.*, **122**, 2202–2209, https://doi.org/10.1175/1520-0493(1994)122<2202:EATFFM>2.0.CO;2.

Newsom, R., W. Brewer, J. Wilczak, D. Wolfe, S. Oncley, and J. Lundquist, 2017: Validating precision estimates in horizontal wind measurements from a Doppler lidar. *Atmos. Meas. Tech.*, **10**, 1229–1240, https://doi.org/10.5194/amt-10-1229-2017.

Pearson, G., F. Davies, and C. Collier, 2009: An analysis of the performance of the UFAM pulsed Doppler lidar for observing the boundary layer. *J. Atmos. Oceanic Technol.*, **26**, 240–250, https://doi.org/10.1175/2008JTECHA1128.1.

Petterssen, S., 1936: A contribution to the theory of frontogenesis. *Geofys. Publ.*, **11**, 1–27.

Rochette, L., W. L. Smith, M. Howard, and T. Bratcher, 2009: ASSIST, Atmospheric Sounder Spectrometer for Infrared Spectral Technology: Latest development and improvement in the atmospheric sounding technology. *Proc. SPIE*, **7457**, 745702, https://doi.org/10.1117/12.829344.

Rodgers, C. D., 2000: *Inverse Methods for Atmospheric Sounding: Theory and Practice*. Series on Atmospheric, Oceanic, and Planetary Physics, Vol. 2, World Scientific, 238 pp.

Rotunno, R., and J. Klemp, 1985: On the rotation and propagation of simulated supercell thunderstorms. *J. Atmos. Sci.*, **42**, 271–292, https://doi.org/10.1175/1520-0469(1985)042<0271:OTRAPO>2.0.CO;2.

Santanello, J. A., C. D. Peters-Lidard, S. V. Kumar, C. Alonge, and W.-K. Tao, 2009: A modeling and observational framework for diagnosing local land-atmosphere coupling on diurnal time scales. *J. Hydrometeor.*, **10**, 577–599, https://doi.org/10.1175/2009JHM1066.1.

Sisterson, D. L., R. A. Peppler, T. S. Scress, P. J. Lamb, and D. D. Turner, 2016: The ARM Southern Great Plains (SGP) site. *The Atmospheric Radiation Measurement (ARM) Program: The First 20 Years*, Meteor. Monogr., No. 57, Amer. Meteor. Soc., https://doi.org/10.1175/AMSMONOGRAPHS-D-16-0004.1.

Smith, T. L., S. G. Benjamin, J. M. Brown, S. Weygandt, T. Smimova, and B. Schwartz, 2008: Convection Forecasts from the Hourly Updated, 3-km High Resolution Rapid Refresh model. *24th Conf. on Severe Local Storms*, Savannah, GA, Amer. Meteor. Soc., 11.1, https://ams.confex.com/ams/24SLS/techprogram/paper_142055.htm.

Spencer, P. L., and C. A. Doswell, 2001: A quantitative comparison between traditional and line integral methods of derivative calculation. *Mon. Wea. Rev.*, **129**, 2538–2554, https://doi.org/10.1175/1520-0493(2001)129<2538:AQCBTA>2.0.CO;2.

——, P. R. Janish, and C. A. Doswell, 1999: A four-dimensional objective analysis scheme and multitriangle technique for wind profiler data. *Mon. Wea. Rev.*, **127**, 279–291, https://doi.org/10.1175/1520-0493(1999)127<0279:AFDOAS>2.0.CO;2.

Sutcliffe, R. C., 1939: Cyclonic and anticyclonic development. *Quart. J. Roy. Meteor. Soc.*, **65**, 518–524, https://doi.org/10.1002/qj.49706528208.

Turner, D. D., and U. Löhnert, 2014: Information content and uncertainties in thermodynamic profiles and liquid cloud properties retrieved from the ground-based Atmospheric Emitted Radiance Interferometer (AERI). *J. Appl. Meteor. Climatol.*, **53**, 752–771, https://doi.org/10.1175/JAMC-D-13-0126.1.

——, and R. G. Ellingson, 2016: Introduction. *The Atmospheric Radiation Measurement Program: The First 20 Years*, Meteor. Monogr., No. 57. Amer. Meteor. Soc., https://journals.ametsoc.org/view/journals/amsm/57/1/amsm.57.issue-1.xml.

——, and W. G. Blumberg, 2019: Improvements to the AERIoe thermodynamic profile retrieval algorithm. *IEEE J. Sel. Top. Appl. Earth Obs. Remote Sensing*, **12**, 1339–1354, https://doi.org/10.1109/JSTARS.2018.2874968.

Wulfmeyer, V., and Coauthors, 2018: A new research approach for observing and characterizing land–atmosphere feedback. *Bull. Amer. Meteor. Soc.*, **99**, 1639–1667, https://doi.org/10.1175/BAMS-D-17-0009.1.

Zamora, R. J., M. A. Shapiro, and C. A. Doswell III, 1987: The diagnosis of upper tropospheric divergence and ageostrophic wind using profiler wind observations. *Mon. Wea. Rev.*, **115**, 871–884, https://doi.org/10.1175/1520-0493(1987)115<0871:TDOUTD>2.0.CO;2.